A 3D Mesoscale Damage-Plasticity Approach for Masonry Structures under Cyclic Loading

Eleni Minga · Lorenzo Macorini · Bassam A. Izzuddin

Abstract This paper deals with the accurate modelling of unreinforced masonry (URM) behaviour using a 3D mesoscale description consisting of quadratic solid elements for masonry units combined with zero-thickness interface elements, the latter representing in a unified way the mortar and brick-mortar interfaces. A new constitutive model for the unified joint interfaces under cyclic loading is proposed. The model is based upon the combination of plasticity and damage. A multi-surface yield criterion in the stress domain governs the development of permanent plastic strains. Both strength and stiffness degradation are captured through the evolution of an anisotropic damage tensor, which is coupled to the plastic work produced. The restitution of normal stiffness in compression is taken into account by employing two separate damage variables for tension and compression in the normal direction. A simplified plastic yield surface is considered and the coupling of plasticity and damage is implemented in an efficient step by step approach for increased robustness. The computational cost of simulations performed using the mesoscale masonry description is reduced by employing a partitioning framework for parallel computation, which enables the application of the model at structural scale. Numerical results are compared against experimental data on realistic masonry components and structures subjected to monotonic and cyclic loading to show the ability of the proposed strategy to accurately capture the behaviour of URM under different types of loading.

1 Introduction

The behaviour of URM - as of any composite material - is influenced by a large variety of parameters including the characteristics of its constituents, the interaction between them and their spatial arrangement - i.e. the mesostructure. Each of these parameters has a distinct effect on the macroscopic behaviour of the material, rendering the prediction of its response a challenging task.

Macroelements are often used to account for the influence of URM components in heterogeneous structures - such as infill frames - or for the modelling of bare URM systems [1, 2, 3]. This phenomenological approach, used for its practicality, is overly simplified to provide insight into the various parameters that define the response of masonry. Macroscale constitutive models [4, 5, 6] describe masonry as homogeneous material on a structural scale and are often chosen due to their relative simplicity. However, this approach requires a cumbersome parameter identification process which is not always possible, and it may lead to inaccurate failure mode predictions.

In recent years and as the available computational resources increase, focus has been given to more refined modelling approaches where each constituent of the material - i.e. the brick/blocks, the mortar joints and the block-mortar interface - is represented explicitly. In this case the identification of the model parameters relies on the identification of the basic material

E. Minga
Department of Civil and Environmental Engineering, Imperial College London, SW7 2AZ
E-mail: e.minga13@ic.ac.uk

L. Macorini, B.A. Izzuddin
Department of Civil and Environmental Engineering, Imperial College London, SW7 2AZ

properties of each constituent; additionally the influence of the mesostructure is accounted for, resulting in a more generic representation. Mesoscale masonry models usually consist of continuum elements for the blocks connected through zero-thickness cohesive interfaces which represent the mortar and the block-mortar interface. In this case the constitutive model employed for the description of fracture in the cohesive interfaces largely determines the characteristics of the nonlinear behaviour of the masonry component.

The first developments of cohesive interface models were based on the pioneering work of Hillerborg [7] on fracture mechanics. In order to simulate the strength degradation and the frictional slip in cracked interfaces of quasi-brittle materials under monotonic loading, models based on pure plasticity can be employed. Among others, Carol et al. [8] implemented 2D formulations purely based on softening plasticity, later extended to a 3D framework [9]. Lourenco et al. [10] presented a similar softening plasticity-based approach in 2D with a multi-surface criterion suitable for masonry joints, which includes a compressive cut-off surface. More refined approaches for cohesive interfaces employed to investigate the monotonic response of masonry include the work by Snozzi et al. [11] who proposed a traction-separation constitutive law for mode I and mode II fracture combined with a frictional contact/impact algorithm ruling the behaviour after decohesion.

When modelling the cyclic behaviour of a frictional interface, more factors have to be accounted for, such as stiffness degradation, permanent strains and hysteresis. Oliveira et al. [12] developed a cyclic 2D model purely based on multi-surface plasticity. Aref et al. [13] implemented a 3D softening plasticity formulation allowing for stiffness degradation in the normal direction in a simplified way, through one parameter. However, the combination of plasticity and damage can offer a more practical and flexible framework for the description of cyclic cohesive interface behaviour.

Models based on micromechanical considerations of damage mechanics [14, 15, 16], apply a decomposition of stresses in two components referring to the damaged and undamaged part of the interface. Inelastic strains are associated with the former stress component to represent the crack opening and/or the slip in the damaged part of the interface. In this framework, Sacco et al. [14] compute the inelastic strains using Coulomb friction in shear and unilateral contact in the normal direction, while Ragueneau et at. [15] employ a plastic criterion with kinematic hardening to reproduce hysteretic cycles in tension and residual strains. Recently, the work in [14] has been extended to micro-plane kinematics to

take into account asperities of the cracked interfaces [17].

Plasticity and damage have also been combined with a standard plastic decomposition of strains to an elastic and an inelastic component. Gambarotta et al. [18] developed a 2D model where the evolution of the inelastic strains is coupled to the evolution of a damage variable. Despite the efficient representation of local cyclic behaviour characteristics, excessive hysteretic dissipation is observed in the numerical-experimental comparisons on the response of walls subjected to shear forces [18]. Grassl at al. [19] developed a 3D interface material model for the cyclic behaviour of frictional interfaces in the mesostructure of concrete. Using a standard plastic formulation it introduces a damage variable to the tangent stiffness decoupling the solution of the plastic problem from the damage evolution.

In this work, a novel material model combining plasticity and damage is proposed to represent the cyclic behaviour of unified joints and cracking surfaces of masonry units in a 3D mesoscale masonry model. Due to the generally large size of 3D mesoscale numerical models and the consequent spread of local effects especially in the case of cyclic loading, one of the main concerns is the development of a robust interface constitutive model that requires a small number of iterations for the local solution and achieves convergence for large strain increments. The proposed model employs a simplified multi-surface plasticity criterion for cohesive interfaces based on experimental evidence on masonry joints. The plastic problem involving only hardening ensures a robust solution in the sense described above. The effects of strength and stiffness degradation are introduced through an anisotropic damage tensor which develops as a function of the plastic work based on specific assumptions on the damage evolution in the joints. An algorithmic decoupling of plasticity and damage, as proposed in Grassl et al. [19], is employed. Therefore, no further local iterations are required after the solution of the plastic problem. The model captures the main characteristics of the cyclic behaviour of masonry joints under cyclic loading in a simple but efficient way and it can be used for the investigation of the behaviour of relatively large masonry components or structural systems.

In the following, a short description of the adopted mesoscale model is provided and the partitioning framework in which the mesoscale description is incorporated is briefly outlined. Subsequently, the formulation of the interface constitutive model is presented in detail in two separate sections corresponding to the two phases of the local solution: multi-surface plasticity and damage. The equations related to the iterative solution algo-

rithm are then provided and the robustness of the local solution is investigated. A section of representative numerical examples follows, showing the performance of the mesoscale masonry model under a range of loading scenarios and its potential for the simulation of URM structural components and systems.

2 Partitioned mesoscale model for masonry

The mesoscale description adopted here was initially proposed in [20] and is based on certain observations on the type of damage that masonry sustains. Firstly, the material nonlinearity and the potential cracking paths of masonry are mostly concentrated in the mortar joints. The thickness of these zones with respect to the dimensions of the masonry component is adequately small to be neglected. Furthermore, cracks can traverse the blocks, usually at the level of the neighbouring head joints, hence the approximate position of the most probable cracking surface of blocks is known. On the whole, the potential crack paths are practically predefined and localised in very thin zones of the material. Finally, bricks and blocks generally experience small deformations compared to the strains developed along the cracks.

Based on the above assumptions and to obtain a realistic 3D masonry description, the blocks are discretised with 20-noded quadratic solid elements which are assumed elastic. In parallel, the mortar joints and the brick failure surfaces - i.e. the potential crack paths - are modelled by 16-noded zero-thickness cohesive interface elements. This implies that the mortar and the block-mortar interfaces are modelled in a unified way by one joint interface element, as shown in Figure 1. The dimensions of the solid elements representing masonry units are expanded to cover the area of the mortar joints.

Since the material model employed for the solid elements is linear elastic, the 16-noded interface elements are designed to account for material nonlinearity in the mesoscale masonry model. The geometric nonlinearity is treated with the use of Green strains for the solid elements and a co-rotational approach for the interface elements, in which the local reference system of the zero-thickness interface moves together with the mid-plane of the element [21, 22]. The nonlinear material behaviour is presented in the following section. For details on the implementation of the interface elements the reader is referred to [22].

The 3D mesoscale description enables a realistic representation of any masonry bonding pattern - considering both the in-plane and the through-thickness geometry - as well as non-planar masonry structures such
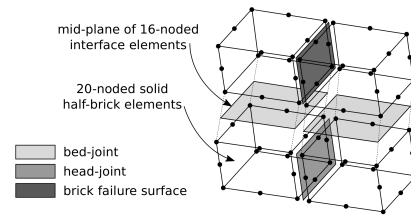

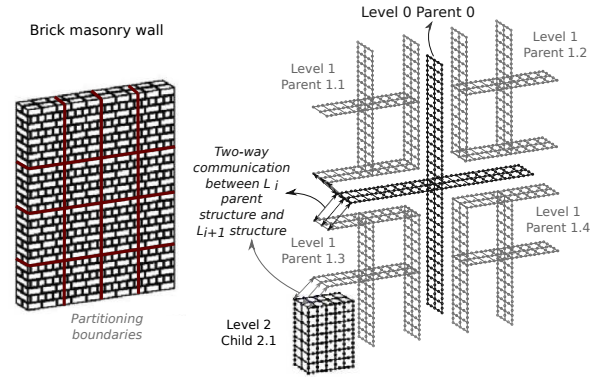**Fig. 1** Mesoscale modelling of brick masonry

Fig. 2 Modelling with hierarchic partitioning

as arches and domes. The main shortcoming of this modelling strategy is the increased computational cost, which usually restricts the use of mesoscale models to small-scale applications. As presented in previous work [23], one strategy that can be used to tackle this limitation and increase the applicability of the model is the use of domain decomposition and parallel processing. This approach is applied in the present work; the mesoscale masonry models are divided in several partitions which are analysed in parallel using different processors. Dual super-elements - consisting of i) the nodes on the partition boundaries [24] or ii) a set of master nodes coupled to the latter [25] - are defined as parent structures. The super-elements achieve a two-way communication between the partitions through an interface displacement frame method at the level of the parent structure. They also allow the hierarchic partitioning of the structure, as illustrated in Fig.2, which results in further improvement of the performance.

3 Interface constitutive model

The constitutive model presented here defines the relation between the local stress and strain variables at each Gauss point of the 16-noded interface element; these are the interface tractions (stress measure) and the interface relative displacements between initially coinciding nodes (strain measure). The stress and strain measures

consist of three components corresponding to the normal and the two tangential directions defined according to the element local reference system on the interface mid-plane (x,y,z) [22], shown in Fig. 3. They will be denoted in the following by:

$$\boldsymbol{\sigma} = \langle \sigma_n, \tau_x, \tau_y \rangle \qquad (1)$$

$$\boldsymbol{\varepsilon} = \langle \varepsilon_n, \varepsilon_x, \varepsilon_y \rangle \qquad (2)$$

where n represents the direction normal to the interface mid-plane (z in Fig. 3). The aim is to model all the principal characteristics of the constitutive behaviour of a mortar joint or a dry frictional interface - when mortar is absent - with an efficient formulation that ensures numerical robustness. The most important of these characteristics are i) the softening behaviour in tension and shear, ii) the stiffness degradation depending on the level of damage, iii) the recovery of normal stiffness in compression and iv) the permanent (plastic) strains at zero stresses when the interface is damaged. Additionally, as the nonlinearity of the model is concentrated in the interface elements, the effect of masonry crushing in compression is taken into account in a phenomenological way, through negative normal plastic strain in the interfaces of the crushed area.

The basis of the developed model is the coupling of plasticity and damage. A combination of an applied damage tensor and a standard decomposition of strains in elastic and plastic components is used, which results in the constitutive relation:

$$\boldsymbol{\sigma} = (\boldsymbol{I} - \boldsymbol{D})\tilde{\boldsymbol{\sigma}} = (\boldsymbol{I} - \boldsymbol{D})\boldsymbol{K}(\boldsymbol{\varepsilon} - \boldsymbol{\varepsilon^p}) \qquad (3)$$

where: $\tilde{\boldsymbol{\sigma}} = \langle \tilde{\sigma}_n, \tilde{\tau}_x, \tilde{\tau}_y \rangle^T$ is the vector of the effective stresses, $\boldsymbol{I}$ the identity matrix, $\boldsymbol{D} = diag\{D_n, D_s, D_s\}$ the damage tensor, $\boldsymbol{K} = diag\{K_n, K_t, K_t\}$ the elastic stiffness matrix, $\boldsymbol{\varepsilon^p} = \langle \varepsilon_n^p, \varepsilon_x^p, \varepsilon_y^p \rangle$ the plastic strain vector.
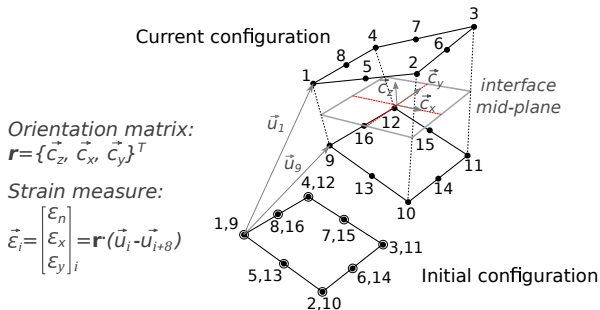

Fig. 3 Interface element kinematics and strain measure

Following the typical notation in damage mechanics, the stress measure $\boldsymbol{\sigma}$ of the interface element will be referred to as "nominal stress". The damage tensor $\boldsymbol{D}$ defines the level of decohesion in each local direction of the interface surface. $\boldsymbol{D}$ is anisotropic, containing distinct variables for the normal and the tangential directions which take values from 0 to 1. The effective stress vector $\tilde{\boldsymbol{\sigma}}$ corresponds to the physical stress developed in the undamaged part of the interface, while the nominal stress $\boldsymbol{\sigma}$ is the physical stress.

The effective stresses $\tilde{\boldsymbol{\sigma}}$ are used in the plastic problem and linked to the plastic deformations $\boldsymbol{\varepsilon^p}$, as given in Eq. 3. The evolution of $\tilde{\boldsymbol{\sigma}}$ is elastic perfectly-plastic or elasto-plastic with linear hardening. Consequently, both the strength degradation - i.e. post-peak softening - and the stiffness degradation of the nominal stresses is produced through damage.

Initially, the plastic problem is solved and $\tilde{\boldsymbol{\sigma}}$ is defined. The plastic work corresponding to each fracture mode is then calculated and used to define the evolution of the damage variables. The damage is finally applied to the effective stresses to obtain the nominal stresses, following Eq. 3. By algorithmically decoupling the implicit solution of the plastic problem and the damage evolution following the idea presented in [19], increased efficiency and robustness is achieved.

3.1 Multi-surface plasticity
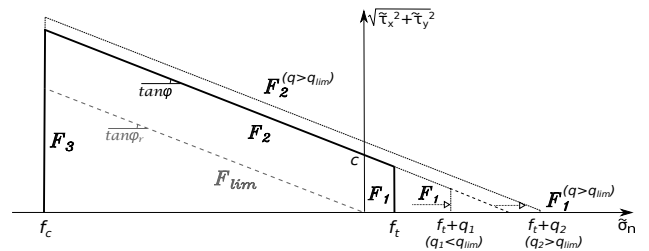
3.1.1 Yield surface

Fig. 4 Multi-surface yield criterion of plastic problem

Based on experimental results [26], the strength of masonry joints under shear can be represented by a Coulomb criterion, defined by the cohesion c and the friction angle ϕ. Thus surface F_2 - depicted in Fig. 4 - was chosen as the plastic yield surface corresponding to mode II fracture:

$$F_2(\tilde{\boldsymbol{\sigma}}) = \sqrt{\tilde{\tau}_x^2 + \tilde{\tau}_y^2} + \tilde{\sigma}_n \tan \phi - c \qquad (4)$$

The conical surface F_2 is capped by two planar surfaces F_1 and F_3. The tensile cap F_1 approximates the

yield surface for mode I fracture, while the compressive cap F_3 approximates the limit beyond which crushing of masonry appears. Planar surfaces were chosen for simplicity and robustness. They are described by the equations:

$$F_1(\tilde{\boldsymbol{\sigma}}, q) = \tilde{\sigma}_n - (f_t + q) \qquad (5)$$

$$F_3(\tilde{\boldsymbol{\sigma}}) = -\tilde{\sigma}_n + f_c \qquad (6)$$

where f_t is the tensile strength of the joint which can be determined through direct tension experiments on joints or through flexural experiments on masonry and f_c is the compressive strength of masonry, which can be easily measured by direct compression experiments. q is a linear hardening variable introduced to control the plastic strains produced in the normal direction under tension - as explained in Section 3.2.3 - and its initial value is zero.

3.1.2 Evolution of yield surface

The evolution of the effective stresses $\tilde{\boldsymbol{\sigma}}$ is elastic perfectly-plastic, except for the case where the plastic surface F_1 is traversed. In this case the evolution of the hardening variable q modifies the yield threshold, as depicted in Fig.4. At a first stage, only surface F_1 evolves. When the hardening variable q reaches the value $q_{lim} = \frac{c}{tan\phi} - f_t$, surface F_1 reaches the edge of the cone F_2 and reduces to a point. Further evolution of q modifies surface F_2 as shown in Fig.4. For $q > q_{lim}$, F_2 is given by the equation:

$$F_2(\tilde{\boldsymbol{\sigma}}, q) = \sqrt{\tilde{\tau}_x^2 + \tilde{\tau}_y^2} + \tilde{\sigma}_n \tan\phi - c' \leq 0 \qquad (7)$$

where:

$$c' = c + (q - q_{lim})tan\phi \qquad (8)$$

3.1.3 Plastic problem

The effective stress vector is given by the state equation:

$$\tilde{\boldsymbol{\sigma}} = \boldsymbol{K}(\varepsilon - \varepsilon^{\boldsymbol{p}}) \qquad (9)$$

Since the yield domain is defined by three surfaces, the plastic strain is given by:

$$\varepsilon^{\boldsymbol{p}} = \varepsilon^{\boldsymbol{p},1} + \varepsilon^{\boldsymbol{p},2} + \varepsilon^{\boldsymbol{p},3} \qquad (10)$$

where $\varepsilon^{\boldsymbol{p},i}$, $i = 1, 3$, is the plastic strain produced through the plastic evolution associated with yield surface F_i.

The second state equation provides the hardening variable and is written as follows:

$$q = -H\kappa \qquad (11)$$

where H is the linear hardening modulus which can be calculated by model parameters, as described in Section 3.2.3.

The evolution of $\varepsilon^{p,1}$ and $\varepsilon^{p,3}$ is based on associated plasticity, thus the plastic potentials G_1 and G_3 coincide with the threshold surfaces F_1 and F_3 respectively. On the contrary, non-associated plasticity is used for the plastic strain $\varepsilon^{p,2}$, in order to control the level of dilatancy of the element under shear loading. The plastic potential G_2 has the same form as F_2 but a different friction angle $tan\phi_g$, generally smaller or tending to zero according to experimental evidence on the dilatancy of masonry joints under shear [26]:

$$G_2(\tilde{\boldsymbol{\sigma}}) = \sqrt{\tilde{\tau}_x^2 + \tilde{\tau}_y^2} + \tilde{\sigma}_n \tan\phi_g - c \qquad (12)$$

Consequently, using standard notation in computational plasticity [27], the flow rules of the plastic problem can be written as follows:

$$\dot{\boldsymbol{\varepsilon}}^{\boldsymbol{p},1} = \dot{\lambda}_1 \frac{\partial F_1}{\partial \tilde{\boldsymbol{\sigma}}}, \quad \dot{\boldsymbol{\varepsilon}}^{\boldsymbol{p},2} = \dot{\lambda}_2 \frac{\partial G_2}{\partial \tilde{\boldsymbol{\sigma}}}, \quad \dot{\boldsymbol{\varepsilon}}^{\boldsymbol{p},3} = \dot{\lambda}_3 \frac{\partial F_3}{\partial \tilde{\boldsymbol{\sigma}}} \quad (13)$$

$$\dot{\kappa} = \dot{\lambda}_1 \frac{\partial F_1}{\partial q} = -\dot{\lambda}_1 \quad (14)$$

where $\dot{\boldsymbol{\varepsilon}}^{\boldsymbol{p},i}$, $i = 1, 3$, is the plastic strain rate and $\dot{\lambda}_i$, $i = 1, 3$, the rate of the plastic multiplier associated with the yield function F_i.

The plastic work produced by the evolution of the plastic strain $\varepsilon^{\boldsymbol{p},i}$ $(i = 1 : 3)$ through the corresponding yield surface F_i, is defined as:

$$W_{pl,i} = \tilde{\boldsymbol{\sigma}} \cdot \boldsymbol{\epsilon}^{\boldsymbol{p},i} \qquad (15)$$

A plastic work variable is associated with each one of the three main deformation modes of the interface - $W_{pl,1}$ for tension, $W_{pl,2}$ for shear and $W_{pl,3}$ for compression.

3.2 Damage evolution

The damage of the interface is defined by three scalar damage variables: D_{nt} for the normal direction in tension, D_{nc} for the normal direction in compression and D_s for the two tangential directions. Those variables compose the diagonal damage tensor $\boldsymbol{D}$.

$$\boldsymbol{D} = \begin{bmatrix} D_n & 0 & 0 \\ 0 & D_s & 0 \\ 0 & 0 & D_s \end{bmatrix}, \text{ with } \quad D_n = \begin{cases} D_{nt}, \text{ if } \tilde{\sigma} \geq 0 \\ D_{nc}, \text{ if } \tilde{\sigma} < 0 \end{cases} \quad (16)$$

The decomposition of the damage variable in the normal direction allows the recovering of the normal elastic stiffness after the closure of the cracks - i.e. in compression - as shown in Fig.7. The damage tensor applied to

the effective stresses provides the nominal stress vector of the interface:

$$\boldsymbol{\sigma} = (\mathbf{I} - \boldsymbol{D})\tilde{\boldsymbol{\sigma}} \tag{17}$$

3.2.1 Assumptions and evolution functions

The damage variables develop with the evolution of the plastic work. Three separate material parameters $G_{f,i}$ ($i = 1, 3$) are introduced, each one corresponding to the fracture energy of the respective fracture/crushing mode associated with a specific yield function. The fracture energy defines the point of complete damage in the respective mode. In the proposed description, the evolution law of the components of $\boldsymbol{D}$ is based on the ratios:

$$r_i = \frac{W_{pl,i}}{G_{f,i}}, \quad i = 1, 3 \tag{18}$$

with $0 \leq r_i \leq 1$.

Physically, the damage of the interface in the tensile or shear mode influences the behaviour under both tension and shear, but it has no significant influence on the response under compression. On the contrary, the behaviour in shear is influenced by the crushing in compression. Based on the above assumptions, the damage variable for the normal direction in tension D_{nt} depends on the plastic work ratios r_1 and r_2. The damage variable for the tangential directions depends on the plastic work ratios of all fracture/crushing modes. Finally, the variable for the normal direction in compression D_{nc} only depends on the plastic work ratio r_3.

The form of the evolution laws of the damage variables as functions of r_i defines the shape of the softening branch of the $\boldsymbol{\sigma} - \boldsymbol{\varepsilon}$ relation. It is noted that the choice of the evolution law is free, thus any law could be devised to refine the representation of the post-peak behaviour. The laws chosen here are described in the following three sections for each component of $\boldsymbol{D}$. Two types of functions are employed therein - a polynomial and a sinusoidal evolution, plotted in Fig.5 and given by the relations:

$$\begin{aligned} F_p(r_i) &= r_i(2 - r_i) \\ F_{sin}(r_i) &= \frac{1}{2}[sin(\pi r_i - \frac{\pi}{2}) + 1] \end{aligned} \tag{19}$$

The second order polynomial $F_p(r_i)$ is used in the evolution laws of D_{nt} and D_s, as it effectively reproduces the abrupt drop in strength after the crack opening in tension and shear [26, 28, 29]. Conversely, the post-peak behaviour of masonry under compression is characterised by a gradually increasing softening [30], which is better approximated by the sinusoidal evolution $F_{sin}(r_i)$.

3.2.2 Damage variable in tension

Let d_t be a measure of the damage evolution when the normal effective stress is elastic-perfectly plastic - i.e when H=0. Then:

$$d_t = F_p(r_1) + a_t F_p(r_2)[1 - F_p(r_1)] \tag{20}$$

where the coefficient a_t ($0 \leq a_t \leq 1$) controls the influence of Mode II (shear) plastic work in the tensile damage. The evolution law in Eq.20 for pure tension results in the softening branch in the nominal stresses presented in Fig.6. The nominal stress evolution in tension has to be independent from the hardening variable, the unique purpose of which is to control the level of plastic strains. Therefore, the following criterion must be satisfied:

$$\sigma_n^{(H=0)} = \sigma_n^{(H>0)} \Rightarrow$$
$$(1 - d_t)\tilde{\sigma}_n^{pp} = (1 - D_{nt})(\tilde{\sigma}_n^{pp} + q) \tag{21}$$

In Eq. 21, $\tilde{\sigma}_n^{pp}$ is the elastic perfectly-plastic normal effective stress and D_{nt} is the damage variable that has to be applied to the hardening effective stress in order to obtain the same nominal stress. By manipulation of Eq. 21, the relation providing the damage variable in tension as a function of the hardening variable q can be obtained:

$$D_{nt} = \frac{F_p(r_1)f_t + q}{f_t + q} + a_t F_p(r_2)[1 - \frac{F_p(r_1)f_t + q}{f_t + q}] \tag{22}$$

In case of no hardening ($q = 0$), Eq.22 reduces to Eq.21.

3.2.3 Control of permanent strains and stiffness degradation in the normal direction

As mentioned before, the hardening variable associated with the plastic surface F_1 is introduced to control the level of normal plastic strain in tension. This is deemed necessary since the normal component of the strain ε_n represents crack opening and the cracks in the mortar joints close upon load inversion. The permanent normal
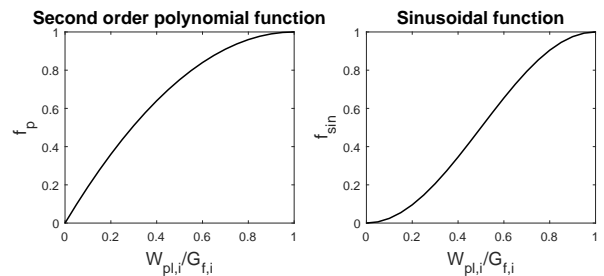

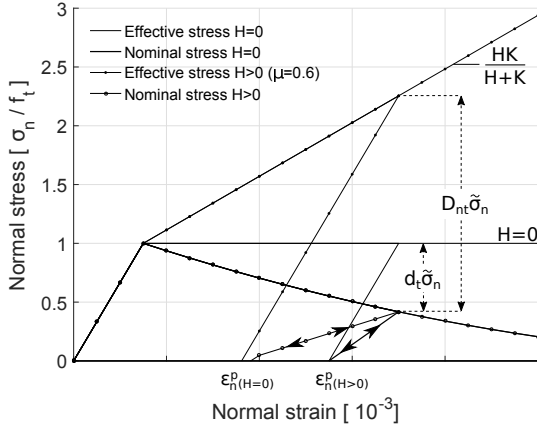**Fig. 5** Functions used in damage evolution laws

Fig. 6 Control of stiffness degradation in the normal direction through hardening

Fig. 7 Definition of model parameter μ

strain after the closure of the cracks might vary depending on the materials and the thickness of the joint; usually in quasi-brittle materials the residual normal strain is small compared to the maximum crack opening attained in the cycle [29]. Additionally, since the model assumes elastic unloading, the level of permanent normal strains at the point of crack closure determines the level of normal stiffness degradation of the damaged interface.

As shown in Fig.6, the value of the hardening modulus H regulates the amount of normal plastic strain ε_n^p produced at a given level of crack opening; as the value of the hardening modulus increases the level of normal plastic strain produced at a given ε_n decreases. In the proposed model, material parameter μ is introduced to control the value of H and hence the level of permanent strains upon unloading.

Let ε_f be the normal strain at which full damage in mode I is attained under pure tension, when $D_{nt} = 1$. Let $\varepsilon_n^{p,f}$ be the plastic strain when unloading from that point, as depicted in Fig.7. Parameter μ is defined as the ratio:

$$\mu = \frac{\varepsilon_n^{p,f}}{\varepsilon_f} \tag{23}$$

This ratio is chosen as a material parameter as it is assumed that it can be approximately estimated by experimental cyclic curves in tension. Since $\varepsilon_n^{p,f}$ is the permanent strain upon elastic unloading of the effective stresses, it is given by:

$$\varepsilon_n^{p,f} = \varepsilon_f - \frac{K_n}{\tilde{\sigma}_n} \Rightarrow \varepsilon_n^{p,f} = \varepsilon_f - \frac{K_n}{f_t + H\varepsilon_n^{p,f}} \tag{24}$$

leading to:

$$H = \frac{K_n\epsilon_f(1-\mu) - f_t}{\epsilon_f\mu} \tag{25}$$

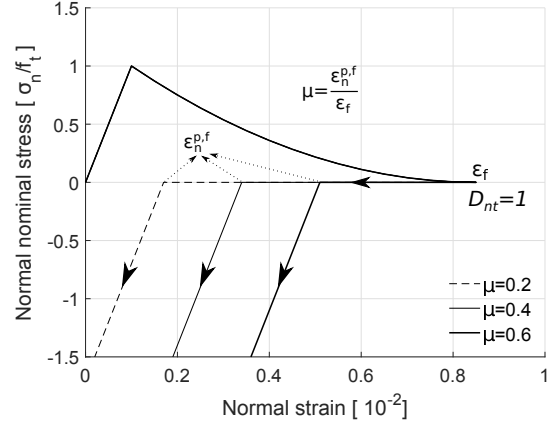The fully damaged state in pure tension corresponding to crack opening equal to ε_f is the point where the plastic work of mode I becomes equal to the respective fracture energy $W_{pl,1} = G_{f,1}$. Thus, ϵ_f can be expressed as a function of the material parameter $G_{f,1}$:

$$G_{f,1} = \int_{f_t/K_n}^{\varepsilon_f} \sigma_n d\varepsilon_n \Rightarrow \epsilon_f = \frac{3G_{f,1}}{f_t} + \frac{f_t}{K_n} \tag{26}$$

Consequently, the hardening modulus can be calculated by the following equation as a function of other model parameters:

$$H = \frac{K_n}{(1 + \frac{f_t^2}{3K_nG_{f1}})\mu} - 1 \tag{27}$$

3.2.4 Damage variable in compression

The evolution law of the damage variable D_{nc}, which refers to the normal direction in compression, is written as follows:

$$D_{nc} = \frac{f_c - f_{c,r}}{f_c} F_{sin}(r_3) \tag{28}$$

where $f_{c,r}$ is the residual compressive stress when the damage associated with the crushing mode develops fully. Figure 8 presents an example of the cyclic behaviour in the normal direction in which both damage in tension and compression develop. A small value is given to the compressive strength f_c, for plotting purposes. The value of the remaining relevant parameters are: $K_n = 200MPa$, $\mu = 0.1$, $G_{f,1} = 0.02N/mm$, $G_{f,3} = 0.5N/mm$.

The compressive strain of the joints results in penetration between block elements. In the mesoscale model the blocks are enlarged to cover the volume of the joints. Therefore, the inter-penetration between masonry blocks
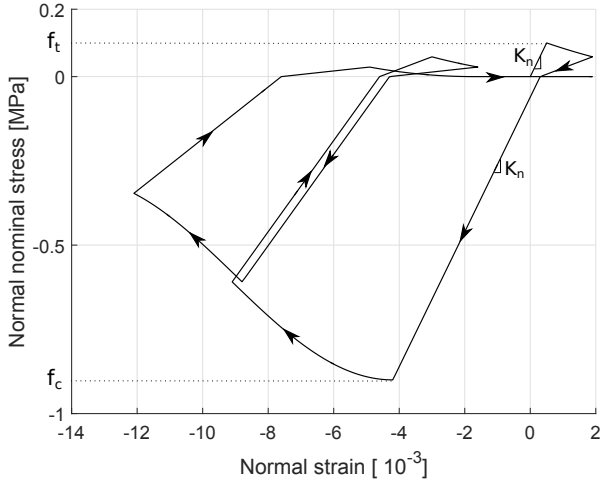
Fig. 8 Cyclic behaviour in the normal direction

is allowed up to the value of the joint thickness. When this value is exceeded, a contact constraint is activated, adding to the normal stiffness of the interface a value equal to the block elastic modulus. The contact constraint - when necessary - is enforced through a penalty parameter at Gauss point level after the convergence of the constitutive model; the consistent stiffness matrix and the internal force vector are updated correspondingly.

3.2.5 Damage variable in tangential direction

Let d_s be a measure of the evolution of damage in the tangential direction at zero normal stress. Then:

$$d_s = a_s \frac{F_p(r_1)c + q_s}{c + q_s}[1 - F_p(r_2) - F_p(r_3) +$$

$$F_p(r_2)F_p(r_3)] + F_p(r_2)(1 - F_p(r_3)) + F_p(r_3) \quad (29)$$

where the coefficient a_s ($0 \leq a_s \leq 1$) controls the influence of mode I plastic work in the tangential damage and q_s describes the hardening in the shear yield threshold when $q > q_{lim}$:

$$q_s = \begin{cases} 0 & , \text{ if } q \leq q_{lim} \\ (q - q_{lim})\tan\phi & , \text{ if } q > q_{lim} \end{cases} \quad (30)$$

In an interface completely damaged in the tangential direction, Coulomb friction with zero cohesion is activated. This residual yield surface corresponds to F_{lim} in Fig. 9, which is described by the equation:

$$F_{lim} = \sqrt{\tilde{\tau}_x^2 + \tilde{\tau}_y^2} + \tilde{\sigma}_n \tan\phi_r \quad (31)$$

The angle ϕ_r represents the residual friction angle of the damaged joint which is usually considered equal to the initial friction angle ϕ. However, it can assume a

lower value if deemed appropriate, for example in the case of dry joints [28].

In order to obtain the residual frictional behaviour described above, the damage variable D_s in the compressive region is defined as a function of the normal stress $\sigma_n < 0$, so that the resulting nominal stresses lay on F_{lim}, as shown in Fig.9. Therefore the value of D_s is given by:

$$D_s = \begin{cases} d_s & , \text{ if } \sigma_n \geq 0 \\ \dfrac{d_s(c + |\sigma_n|(\tan\phi - \tan\phi_r))}{c + |\sigma_n|\tan\phi} & , \text{ if } \sigma_n < 0 \end{cases} \quad (32)$$

The resulting shear behaviour for different levels of compressive strength is presented in Fig. 10.

Fig.11 shows an example of local cyclic behaviour in shear under compressive stress $\sigma_n = -2c$, where c is the cohesion. The fracture energy for mode II employed is $G_{f,2} = 0.2 N/mm$. It is noted that the damage in shear produces only a limited amount of stiffness degradation, which agrees with experimental data on cyclic shear behaviour of masonry joints, according to which the stiffness degradation is not a prevailing factor in shear and is limited to a low level [26, 28].

3.3 Solution procedure and consistent stiffness

Depending on the surfaces activated at each step, the solution of the multi-surface plasticity problem can be divided in five cases: either one single surface is activated ($\alpha = 1, 2, 3$) or two intersecting ones ($\alpha = [1, 2], [2, 3]$). In each case the system of equations that has to be solved for step κ can be written in residual form as follows:

$$\begin{cases} \boldsymbol{R}_{\tilde{\sigma},\kappa} = \tilde{\boldsymbol{\sigma}}_\kappa - \tilde{\boldsymbol{\sigma}}_{\kappa-1} - \boldsymbol{K}(d\boldsymbol{\varepsilon}_\kappa - d\lambda_{a,\kappa}\frac{\partial G_a}{\partial \tilde{\boldsymbol{\sigma}}}|_\kappa) = \boldsymbol{0} \\ R_{q,\kappa} = q_\kappa - q_{\kappa-1} - Hd\lambda_{1,\kappa} = 0 \\ \boldsymbol{R}_{F_a,\kappa} = F_a(\tilde{\boldsymbol{\sigma}}_\kappa, q_\kappa) = \boldsymbol{0} \end{cases} \quad (33)$$

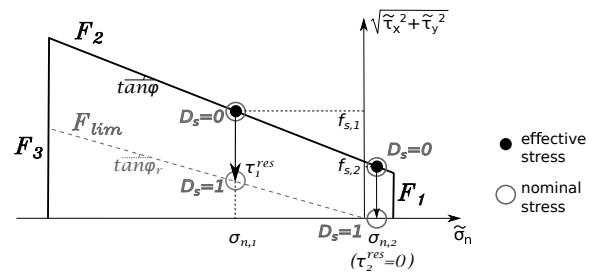where the indice a implies repetition for all the active surfaces.

Fig. 9 Shear stress residual based on Coulomb friction (f_s=yield tangential stress, τ^{res}=residual tangential stress for different levels of compression)
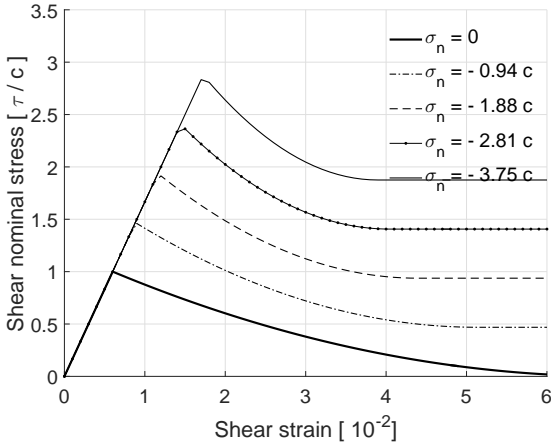
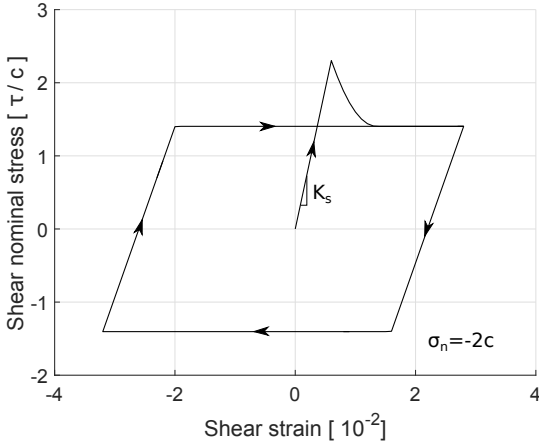**Fig. 10** Shear behaviour at different levels of normal stress

Fig. 11 Cyclic behaviour under shear

When only one planar surface - F_1 or F_3 - is activated the system is linear and is readily solved without an iterative procedure. When the system (33) is non-linear, it is solved with a full Newton-Raphson scheme. Since the second equation in (33) is always readily solved, $q_\kappa = q_{\kappa-1} + H d\lambda_{1,\kappa}$ is replaced in the remaining equations and the system is linearised:

$$\boldsymbol{R}_\kappa^{(i)} = \boldsymbol{R}_\kappa^{(i-1)} + \boldsymbol{J}_\kappa^{(i-1)} \left[\delta\tilde{\boldsymbol{\sigma}}_\kappa^T \quad \delta d\lambda_{a,\kappa} \right]^{(i),T} = 0$$
$$\Rightarrow \left[\delta\tilde{\boldsymbol{\sigma}}_\kappa^T \quad \delta d\lambda_{a,\kappa} \right]^{(i),T} = -[\boldsymbol{J}_\kappa^{(i-1)}]^{-1} \boldsymbol{R}_\kappa^{(i-1)} \quad (34)$$

where $\boldsymbol{R}_\kappa = [\boldsymbol{R}_{\tilde{\boldsymbol{\sigma}},\kappa}^T \quad \boldsymbol{R}_{F_a,\kappa}^T]^T$ and the Jacobian matrix $\boldsymbol{J}_\kappa^{(i)}$ is written:

$$\boldsymbol{J}_\kappa^{(i)} = \left. \begin{bmatrix} \frac{\partial \boldsymbol{R}_{\tilde{\boldsymbol{\sigma}},\kappa}}{\partial \tilde{\boldsymbol{\sigma}}_\kappa} & \frac{\partial \boldsymbol{R}_{\tilde{\boldsymbol{\sigma}},\kappa}}{\partial d\lambda_{a,\kappa}} \\ \frac{\partial \boldsymbol{R}_{F_a,\kappa}}{\partial \tilde{\boldsymbol{\sigma}}_\kappa} & \frac{\partial \boldsymbol{R}_{F_a,\kappa}}{\partial d\lambda_{a,\kappa}} \end{bmatrix} \right|_{(i)} \quad (35)$$

The unknowns are updated at each step of the iterative procedure of the Newton-Raphson scheme:

$$\begin{bmatrix} \tilde{\boldsymbol{\sigma}}_\kappa \\ d\lambda_{a,\kappa} \end{bmatrix}^{(i)} = \begin{bmatrix} \tilde{\boldsymbol{\sigma}}_\kappa \\ d\lambda_{a,\kappa} \end{bmatrix}^{(i-1)} + \begin{bmatrix} \delta\tilde{\boldsymbol{\sigma}}_\kappa \\ \delta d\lambda_{a,\kappa} \end{bmatrix}^{(i)} \quad (36)$$

until the normalisation of the residual $[\delta\tilde{\boldsymbol{\sigma}}_\kappa^T \quad \delta d\lambda_{a,\kappa}]^{(i)}$ becomes smaller to the chosen tolerance.

After the plastic problem has been solved, the plastic work of each fracture mode and the ratio with respect to the corresponding fracture energy are calculated by Eq.15 and 18 respectively. Subsequently, the damage variables can be evaluated, as described in Sections 3.2.2, 3.2.4, 3.2.5, providing the damage tensor $\boldsymbol{D}$.

The consistent stiffness at the end of a converged step κ is given by the following expression:

$$\boldsymbol{K_c} = \left. \frac{\partial \boldsymbol{\sigma}}{\partial \boldsymbol{\varepsilon}} \right|_\kappa = (\boldsymbol{I} - \boldsymbol{D}_\kappa) \left. \frac{\partial \tilde{\boldsymbol{\sigma}}}{\partial \boldsymbol{\varepsilon}} \right|_\kappa - \left. \frac{\partial \boldsymbol{D}}{\partial \boldsymbol{\varepsilon}} \right|_\kappa \tilde{\boldsymbol{\sigma}}_\kappa \quad (37)$$

The partial derivative of the effective stresses with respect to the strain measure can be calculated through the Jacobian of the plastic problem:

$$\boldsymbol{K_c} = \left. \frac{\partial \tilde{\boldsymbol{\sigma}}}{\partial \boldsymbol{\varepsilon}} \right|_\kappa = \boldsymbol{J}_n^{-1} \cdot \boldsymbol{K_e} \quad (38)$$

where $\boldsymbol{K_e} = \left[\boldsymbol{K}^T \quad \boldsymbol{0}_{[3\times(s-3)]} \right]^T$ and s is the size of $\boldsymbol{J_\kappa}$.

The calculation of the variation of the damage tensor with respect to the strain measure involves separate chain derivations for each component of the tensor, following the pattern below:

$$\left. \frac{\partial \boldsymbol{D}}{\partial \boldsymbol{\varepsilon}} \right|_\kappa = \left. \frac{\partial \boldsymbol{D}}{\partial W_{pl,a}} \left(\frac{\partial W_{pl,a}}{\partial \tilde{\boldsymbol{\sigma}}} \frac{\partial \tilde{\boldsymbol{\sigma}}}{\partial \boldsymbol{\varepsilon}} + \frac{\partial W_{pl,a}}{\partial \boldsymbol{\varepsilon}^{p,i}} \frac{\partial \boldsymbol{\varepsilon}^{p,i}}{\partial \boldsymbol{\varepsilon}} \right) \right|_\kappa \quad (39)$$

where the indices a and i imply summation of the products over the active set of the respective variables.

3.4 Robustness of local solution

The simplicity of the yield criterion and the absence of softening are two choices made to increase the robustness of the local solution. The result is investigated in simple tests applying specific strain increments at Gauss point level and examining the convergence and number of iterations required for the local solution. The input strain increments are chosen to give rise to trial stress vectors that have a specific direction in the σ_n, τ surface, as depicted in Fig.12(a). A range of angles θ from $0°$ to $90°$ have been tested. For each angle, the first increment produces a trial stress that reached to the edge of the yield domain. Subsequently, the increment is multiplied by 10 until the multiplier reaches the value $N = 10^6$. The tolerance used in this test is 10^{-8}.
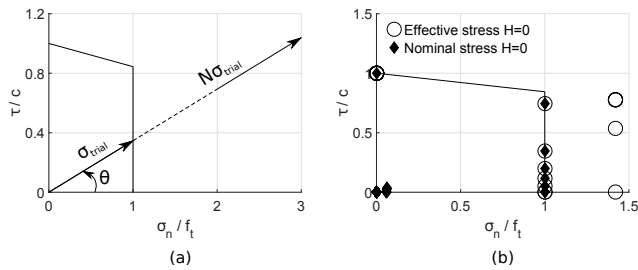
Fig. 12 (a) Trial stress vectors for robustness test; (b) Converged effective and nominal stresses

Table 1 Convergence of solution algorithm at the Gauss point level

θ	$0°$	$15°$	$30°$	$45°$	$60°$	$75°$	$90°$
$N = 10^0$	0	0	0	0	0	0	0
$N = 10^1$	1	1	2	2	2	2	2
$N = 10^2$	1	2	2	2	2	2	2
$N = 10^3$	1	2	2	2	2	2	2
$N = 10^4$	1	2	2	2	2	2	2
$N = 10^5$	1	2	2	2	2	2	2
$N = 10^6$	1	2	2	2	2	2	2

The test results regarding the number of iterations required for the solution of the local problem are reported in Table 1. It is observed that convergence is achieved in all cases. When the planar surface F_1 is activated alone - for example in the loading series with $\theta = 0°$ - the system is linear and is readily solved without an iterative procedure. In this case the solution is obtained invariably, regardless of the strain increment. Furthermore, in the cases where a Newton-Raphson procedure is required (activation of F_2 alone or F_1 and F_2 together), the system can be solved in 2 iterations for multipliers up to $N = 10^6$, which already corresponds to unusually large strain increments. It is thus concluded that for the scope of the model the robustness and efficiency are satisfactory. Fig.12(b) shows the converged stress states of the test series, in terms of effective stresses and nominal stresses.

4 Numerical examples

The proposed mesoscale modelling approach has been implemented in ADAPTIC [31], a general finite element code for nonlinear analysis of structures. In this section, this approach is used in simulations of URM structural elements and systems. Numerical results are compared against experimental data found in the literature to investigate the accuracy of the mesoscale description in respresenting the physical response of URM components subjected to different static and dynamic loading conditions.

Table 2 Wall panels loaded in-plane: material parameters for mortar joints

K_n $[N/mm^3]$	K_t $[N/mm^3]$	f_t $[N/mm^2]$	c $[N/mm^2]$
48.0	21.0	0.04	0.23
$tan\phi$	$tan\phi_g$	f_c $[N/mm^2]$	μ
0.58	0.00	6.2	0.1
$G_{f,1}$ $[N/mm]$	$G_{f,2}$ $[N/mm]$	$G_{f,3}$ $[N/mm]$	
0.05	0.10	1.00	

In all the following simulations the meshes created consist of the minimum number of solid elements that can achieve a full mesoscale representation of the masonry bonding pattern. Therefore, one solid element per brick depth and height is always used. On the contrary, the number of solid elements per brick length varies: four solid elements per brick length are used to model English bond (Sections 4.1 and 4.4), while two solid elements per brick length are used to model running bond (Sections 4.2 and 4.3). The integration in the elastic solid elements is performed using 3x3x3 integration points. For the cohesive interface elements 7x7 Gauss points are used for the integration. The larger number of integration points is necessary to represent potential partial decohesion of a masonry joint. Finally, it is noted that in all the following simulations full coupling of the damage in the normal direction in tension D_{nt} and the damage in the tangential direction D_s is assumed. This is achieved by defining parameters a_t and a_s in Eq.(19) and (28) equal to 1.

4.1 Wall panels under in-plane shear

Firstly, the in-plane cyclic response of the mesoscale model under shear loading is studied though the simulation of experiments performed at the Joint Research Centre of the European community in Ispra, Italy [32]. Two wall panels with different aspect ratios (height/width) have been tested to examine the variation in the failure modes and the behaviour characteristics - such as the dissipation and the ultimate load capacity.

The dimensions of the walls are $1000 \times 1350 mm^2$ and $1000 \times 2000 mm^2$, resulting in aspect ratios of 1.35 and 2.00 respectively. The walls were built with brick-block units of $250 \times 120 \times 55 mm^3$ arranged in a two-wythe thick English bond pattern. The thickness of the joints is $10mm$. The bottom of the walls is connected to a fixed surface through a bed joint. Uniform compressive pres-
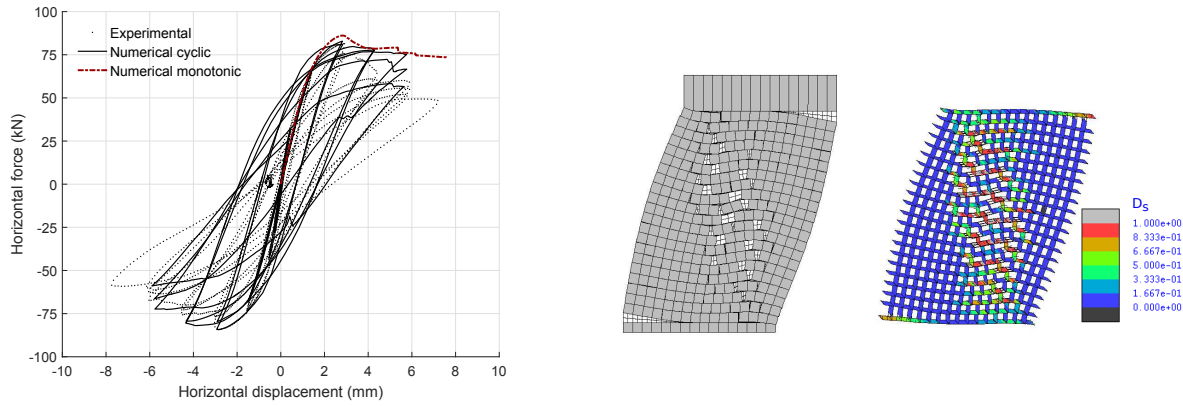
Fig. 13 Short wall under in-plane cyclic loading: experimental-numerical comparison, deformed shape and damage developed in the interfaces
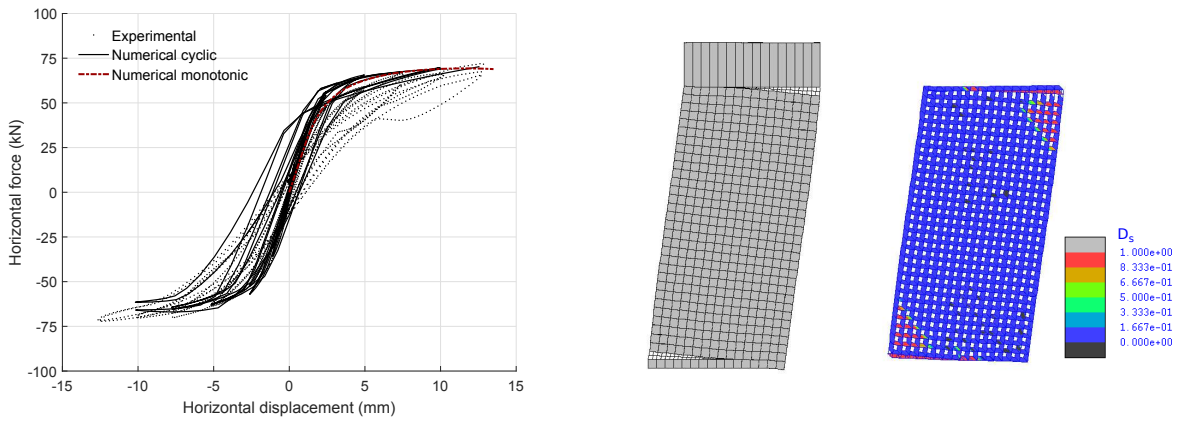

Fig. 14 Tall wall under in-plane cyclic loading: experimental-numerical comparison, deformed shape and damage developed in the interfaces

sure of $0.6MPa$ is applied to each wall through a steel beam on the top. The beam is supported so as to remain horizontal throughout the experiment, providing a slab support. Horizontal in-plane displacement cycles of increasing magnitude are imposed to the beam.

The boundary and loading conditions were modelled in detail, as described above. The mesh developed for the mesoscale representation of the short wall consists of 368 solid elements and 742 interface elements, while the mesh of the tall wall consists of 528 solid elements and 1072 interface elements.

The material parameters of the mesoscale model were chosen based on the experimental results reported in [33], which refer to the same materials used in the construction of the shear walls. The material parameters used in the mesoscale model are summarised in Tables 2 and 3.

The experiments revealed distinct cracking patterns for the two walls [32], which are reproduced by the numerical tests. The main failure mode for the short wall is characterised by shear diagonal cracking spreading

Table 3 Wall panels loaded in-plane: material parameters for brick elements and density of masonry

$E_b[N/mm^2]$	Poisson's ratio	$Density[Kg/m^3]$
3000	0.15	1900

along the height of the panel. Additionally, horizontal cracks and crushing zones appear at the corners. This failure mode is clearly observed in the monotonic analysis, as shown in Fig. 13. The same damage pattern is approximately mirrored on both sides when the wall is subjected to cyclic loading. In the case of the tall wall, the failure mode is in-plane flexure, with cracks appearing in bed joints close to the corners mainly at the top and bottom, as shown in Fig.14 for the monotonic loading. The cyclic response of the tall wall is typical of an in-plane rocking behaviour, which produces a symmetrical cracking pattern at the corners of the wall.

Regarding the force-displacement diagrams presented in Figs 13 and 14, the load at the onset of damage

and the peak load are reproduced with accuracy in both cases. The softening envelope of the short wall is reproduced very accurately in the negative quadrant and reasonably well in the positive quadrant. Furthermore, progressively increasing stiffness degradation is observed at structural level for the short wall. The amount of degradation is less than that obtained experimentally in the first displacement cycles, but the difference is significantly reduced as the damage progresses. Regarding the tall wall, the hardening envelope of the cyclic response is accurately captured and the stiffness degradation and residual displacements are predicted to a satisfactory extent. The numerical analysis results in S-shaped cycles with low dissipation that characterise the behaviour in the first rounds of the experimental test. However, the higher dissipation of the larger displacement cycles that is observed in the experimental curves is not reproduced. This could be partly due to the assumption of elastic unloading-reloading in the proposed constitutive model, which is a simplification of the real unloading-reloading path that might involve a certain level of hysteresis. Additionally, it can be partially explained by the "perfect" symmetrical rocking behaviour produced in the numerical simulations, which cannot appear in an experimental test with a real brick wall, where various effects - such as non-uniform properties of the joints and lack of perfect symmetry - might arise.

4.2 Out-of-plane bending and rocking of wall panels

The out-of-plane flexure and rocking behaviour of single URM wall panels is studied here, based on the simulations of experiments performed by Griffith et al. [34, 35], where simply supported walls with and without pre-compression - representing load bearing and non-load bearing type - were tested under static monotonic loading and dynamic excitations in the out-of-plane direction.

The wall specimens of $110mm$ thickness have a height of $1500mm$ and width of $950mm$, with brick units of dimensions $230 \times 110 \times 76mm^3$. The resulting slenderness ratio (height/ thickness) is 13.6. The mesh generated for the simulation of the wall consists of 144 solid elements and 270 interface elements. The material properties provided in [35] are limited and refer to masonry as a homogeneous material at macroscopic level. The tensile strength of the mortar joints f_t, which is the key parameter for the out-of-plane resistance of the walls, has been calculated by the macroscopic flexural strength of masonry f_{mt} provided in [35] through the simple relation $f_t = \frac{1}{3}f_{mt}$, following the suggestion of Milani [36]. The remaining parameters of the mesoscale model

Table 4 Wall panels out-of-plane: material parameters of mortar joints (new=undamaged joints, dmg=damaged joints)

	K_n [N/mm^3]	K_t [N/mm^3]	f_t [N/mm^2]	$tan\phi$
new	250.0	105.0	0.163	0.24
dmg	10.0	5.0	0.01	0.01
	$tan\phi_g$	c [N/mm^2]	f_c [N/mm^2]	μ
new	0.00	0.75	13.4	0.1
dmg	0.00	0.75	13.4	0.1
	$G_{f,1}$ [N/mm]	$G_{f,2}$ [N/mm]	$G_{f,3}$ [N/mm]	
new	0.05	0.10	1.00	
dmg	0.01	0.01	1.00	

Table 5 Wall panels out-of-plane: material parameters of brick elements and density of masonry

$E_b[N/mm^2]$	Poisson's ratio	$Density[Kg/m^3]$
9400	0.15	1900

that are not provided in [35, 34] were derived based on typical values of constituents' properties in newly constructed masonry.

Tests have been performed to both uncracked and cracked wall specimens, the latter having sustained damage in previous rounds of the experimental testing. For the analyses of the cracked walls, the bed joints at the bottom and at mid-height of the wall have been considered severely damaged, by applying different material parameters to the corresponding interface elements. A summary of all the material parameters employed in the mesoscale model is provided in Tables 4 and 5.

The walls are supported in the direction of the loading at the level of the bottom bed joint. The non-load bearing wall has a similar simple support at the top. In the load bearing walls, a stiff beam is placed in unilateral contact with the top of the wall to transfer the vertical loads and provide a slab support. The compressive load is applied through springs. As a result, the level of the load increases as the wall deforms [34]. This condition was modelled by adding spring elements in the vertical direction on top of the slab.

Initially, the static pushover tests were modelled by imposing displacements at the mid-height of the wall to obtain the complete pre- and post-peak force-displacement curve. The pushover envelopes corresponding to the different boundary conditions and material characteristics are accurately reproduced by the mesoscale model, as shown in Fig.15. Both the peak lateral loads i.e. ultimate strength and the corresponding displacements are predicted in detail. Thus the model
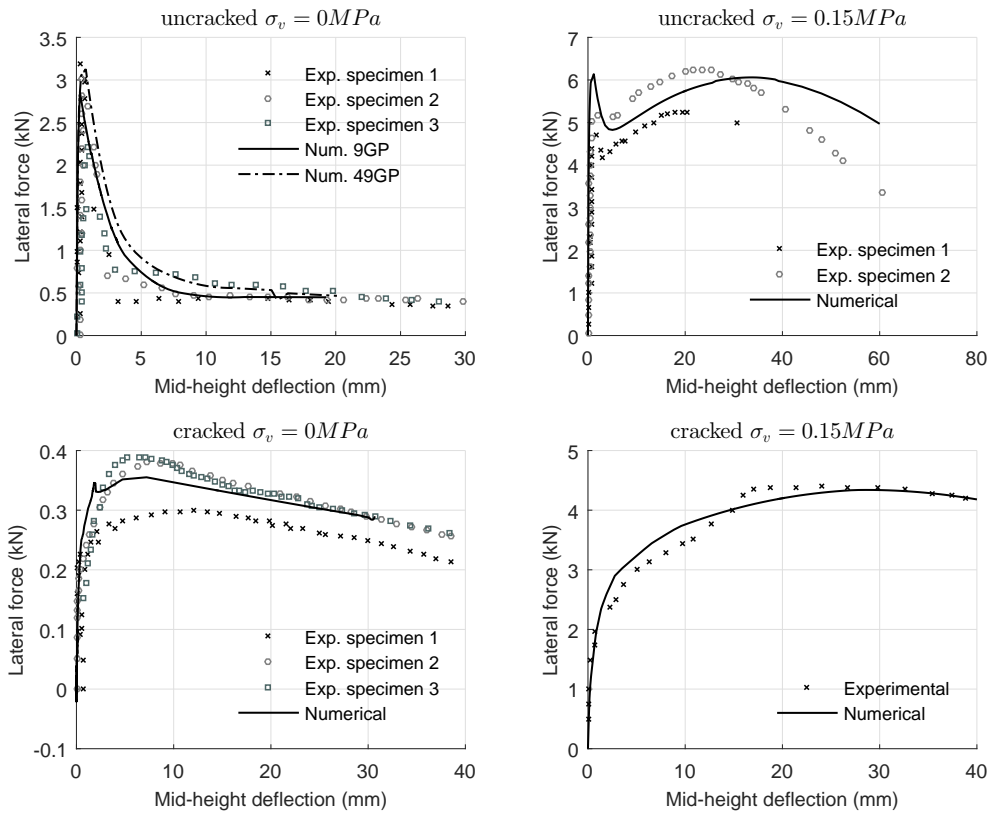
Fig. 15 Walls in out-of plane flexure: experimental numerical comparison of pushover curves
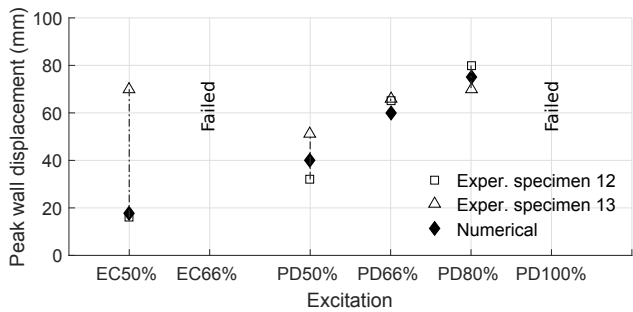

Fig. 16 Rocking out-of-plane: experimental-numerical comparison of PWD for different excitations (EC=El Centro, PD=Pacoima Dam)

gives a complete picture of the flexure response overcoming the limitations of the classical simplified theories of linear elastic and rigid body analysis, which are highlighted in [34].

Subsequently, the shaking table tests with real earthquake excitations were simulated. The top and bottom of the walls were subjected simultaneously to the same out-of-plane accelerations, which correspond to Ground Motion Records (GMR) of two earthquakes - the 1940 El Centro and the 1994 Pacoima Dam earthquake - multiplied by factors from 0.50 to 1.00. As reported in [34], the displacement records produced in the shak-
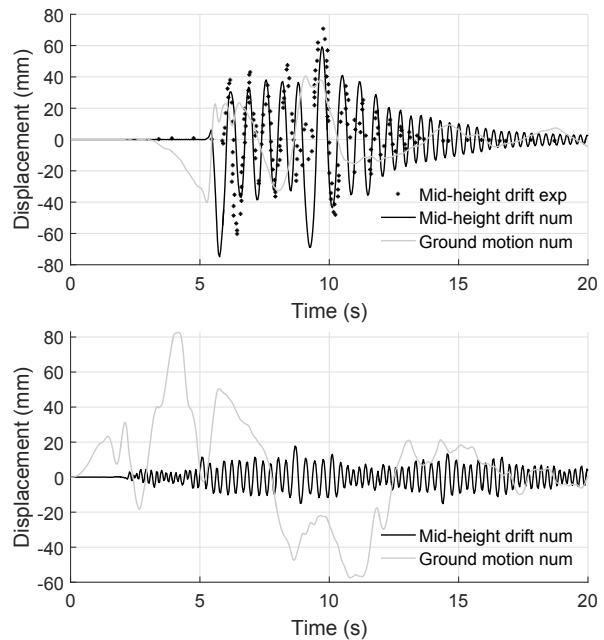

Fig. 17 Rocking out-of-plane: Pacoima Dam 80% excitation (top) and El Centro 50% excitation (bottom)

ing table during the experiments are relatively close to the displacement GMR of the earthquakes but do not coincide. Those tests were performed to cracked spec-

imens, therefore the corresponding material properties reported in Tables 4 and 5 have been employed. In the dynamic analyses, damping is produced through the explicit modelling of the nonlinear material behaviour of the joints.

In [35] experimental results are provided in terms of the Peak Wall Displacement (PWD) of two specimens (12 and 13) for each GMR at different levels of excitation. The PWD corresponds to the out-of-plane drift at the mid-height of the wall. Additionally, response curves are selectively provided for some of the cases.

Fig.16 presents a comparison of the PWD obtained experimentally and numerically for each excitation. Regarding the Pacoima Dam record, the numerical predictions compare well to the experimental observations for every level of excitation and present a clear trend of increasing PWD as the level of excitation increases. The Pacoima Dam record at 100% has produced collapse of the wall both in the numerical and the experimental tests. Regarding the El Centro record, the experimental response of the two specimens at 50% excitation has a large scatter and the numerical result is close to the low response. For accelerations corresponding to 66% of El Centro or higher the wall collapses both in the experimental tests and the numerical simulations.

Fig.17 demonstrates the response curves of the modelled wall under two different excitations: 80% Pacoima Dam and 50% El Centro. The former is compared with the experimental curve given in [34]. For the latter the experimental curve is not available. In each graph the displacement GMR obtained by the numerical analysis is also plotted. A close match is observed between the experimental and numerical results for the 80% Pacoima Dam motion. The small-scale differences could be related to the discrepancy between the real Ground Motion Record and the motion produced by the shaking table. Despite the potential discrepancy, the peak ground acceleration and displacement of the numerical simulation are consistent to the respective values reported in the experiments, which results in the close agreement of the PWD values.

In conclusion, the model can reproduce the dynamic out-of-plane rocking of single wall panels which is based on the opening and closing of the bottom and middle bed joints. Furthermore, a reliable prediction of the out-of-plane drift demand - which defines the capacity of the walls in real earthquake scenarios as suggested in [34] - can be obtained.

4.3 Two-way bending

In real URM structures the boundary conditions of a masonry panel loaded out-of-plane are often more com-
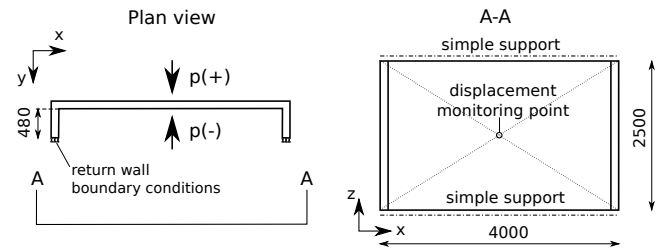

Fig. 18 Two-way bending: geometry and boundary conditions of structure (dimensions in mm)

plicated than those considered in the example above. Commonly, the sides of a wall panel are connected with lateral URM walls through interlocking of the bonding pattern. This arrangement leads to a two-way bending configuration, which has been experimentally tested by Griffith et al. [37]. A numerical simulation has been performed in order to examine the potential of the presented modelling approach for the simulation of larger structural elements, with boundary conditions and interactions that are difficult to take into account with more simplified models.

The specimen 2 in [37] consists of a main wall of $4000 \times 2500mm^2$ without openings and $480mm$ long return walls on both sides, as shown in Fig.18. The mesh employed in this numerical example consists of 1189 solid elements and 2407 interface elements and is divided in 24 partitions. They are built with clay brick units of $230 \times 110 \times 76mm^3$ arranged in running bond. The material properties are similar to the ones in the previous section Table 4-new except for the elastic stiffness parameters of the mortar joints. In order to obtain the elastic modulus of masonry reported in [37], the elastic stiffness values given in Table 6 have been used.

Table 6 Two-way bending URM: material parameters of mortar joints

$K_n[N/mm^3]$	$K_t[N/mm^3]$
80.00	36.00

In the static round of testing, modelled here, uniform pressure is applied at the external face of the main wall (positive direction in Fig. 18), until the ultimate load is exceeded. An unloading phase follows until zero pressure level.

The main wall is simply supported along the top and the bottom edge in the direction of the loading. Additionally, restraints are imposed along the vertical edges of the return walls. The choice of the boundary conditions of the return walls has proven to be crucial
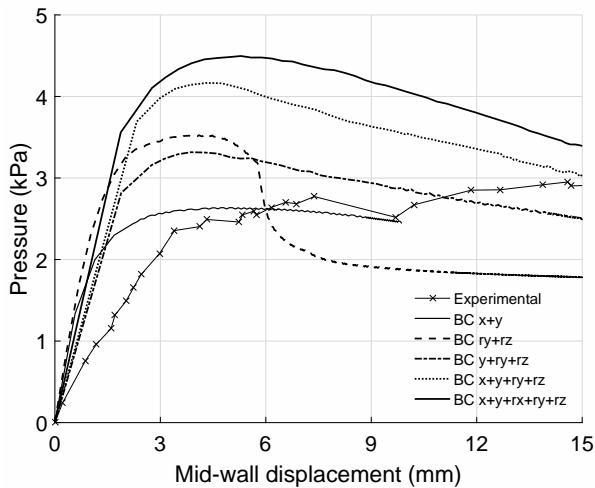
Fig. 19 Two-way bending: study of effect of return walls' boundary conditions in the response

Fig. 20 Two-way bending: experimental-numerical comparison of static series response

for an accurate representation of the actual behaviour of the structure. The exact interpretation in the numerical model of the conditions imposed by the experimental setting described in [37] is not straightforward. For this, a series of different boundary conditions were considered, beginning with the limit cases of fully fixed and simply supported vertical edges. The difference in the load capacity obtained by the limit cases is close to 60% of the experimental value, while the cracking patterns of the return walls and the main wall differ significantly. The sensitivity of the model demonstrates the advantage of detailed modelling of masonry in studying all the characteristics of the structural behaviour and the parameters that affect it. Eventually, it was concluded that the real support is between the limit cases; the boundary conditions approaching closer to the real response - as shown in Fig.19 - is the restraints y+ry+rz at the nodes of the lateral edge of the return walls.

Fig. 20 shows that the global behaviour of the structure obtained numerically with the chosen boundary conditions compares well to the experimental results. The small difference in the initial stiffness probably indicates a discrepancy in the material parameters used in the numerical model and the real values. This is expected since few material parameters, mostly referring to masonry in the macroscale, are reported in [37]. The ultimate load capacity of the wall is captured accurately, within 10% difference to the one obtained experimentally. Additionally, the unloading path indicates an accurate representation of the re-closure of cracks upon unloading. Furthermore, the cracking pattern of the numerical model shown in Fig. 21 compares well with the cracks developed in the wall during the experiment, indicating that the same failure mode is produced.
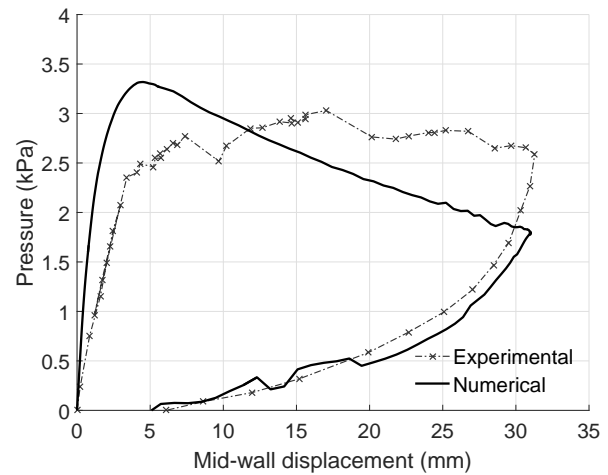
4.4 Perforated wall under cyclic loading in-plane

The final example considered herein, aims to show the potential of the partitioned mesoscale model for the simulation of larger scale structures. For this, part of the experimental tests carried out at the University of Pavia on a real scale masonry building [38] are modelled.

The building has a rectangular plan and is two-storey high. The floors consist of a set of parallel steel joists along the small dimension of the building, which form a very flexible diaphragm. The two longitudinal faces - Wall B and Wall D - include openings. Wall D is not connected to the adjacent lateral walls, hence their influence on the in-plane response of Wall D can be considered minimal. Total dead weight of $248.4KN$ and $236.8KN$ was added to the first and second floor respectively, creating a pre-compression of $0.4 - 0.5MPa$ to the bed joints of the longitudinal walls at ground level. The structure was then subjected to displacement control cyclic loading, with equal horizontal forces applied at each floor level - uniform distribution - in the direction in-plane of Walls B and D, as shown in Fig. 22.

Wall D has been modelled individually, since the influence of the remaining parts of the structure can be neglected. The wall is built in two-wythe thick English bond pattern. The materials are similar to those used in the construction of the two walls in Section 4.1, as the experiments belong to the same larger project. The parameters used in the numerical model are given in Tables 2 and 3.

The mesoscale model of the perforated Wall D is partitioned hierarchically, as shown in Fig.22. Mixed-dimensional coupling was used [25], which drastically
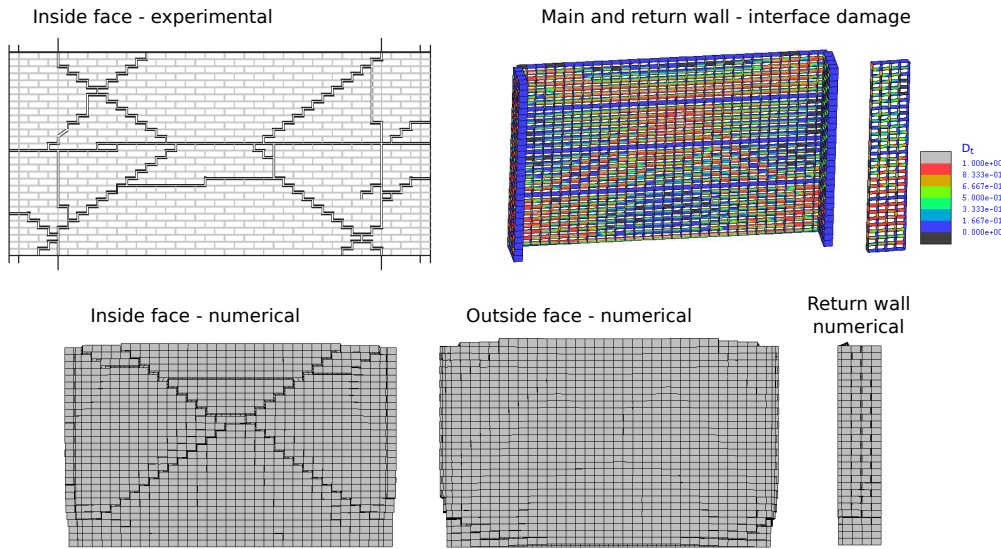
Fig. 21 Two-way bending: damage developed in the interfaces and deformed shape at maximum mid-wall displacement compared to experimental cracking pattern [37]

Table 7 Perforated wall: size of partitioned model

		dofs
nb model nodes:	154920	464760
nb PB nodes:	1115	6690
total	156035	471450

reduces the number of nodes on the partition boundary, further accelerating the analysis. The size of the entire model in terms of number of nodes and degrees of freedom (dofs) is reported in Table 7. Quasi-static displacement-control analysis has been performed, firstly under monotonic loading and subsequently under cyclic loading based on selected peaks of the experimental displacement history.
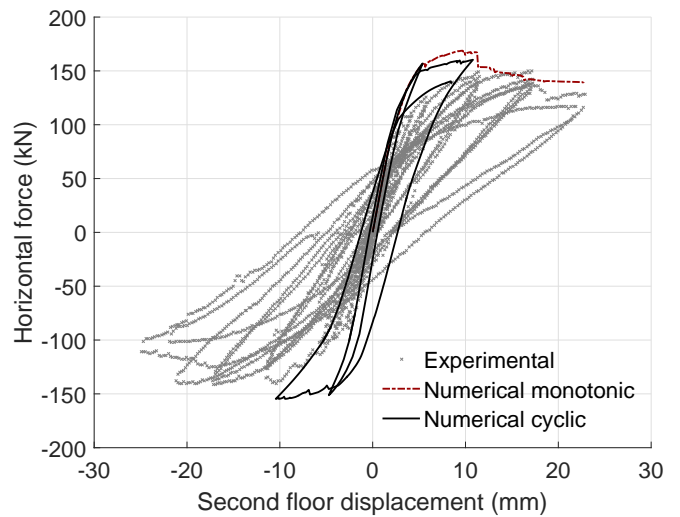

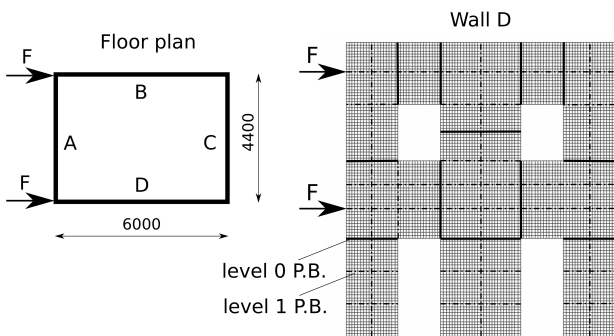**Fig. 23** Perforated wall: experimental-numerical comparison

Fig. 23 presents the comparison of the experimental and numerical results. With the analysis under monotonic loading the pushover curve of the structure is obtained up to the maximum displacement attained during the experiments. It is noted that both increased robustness and reduction of computational time were achieved with the use of the constitutive model proposed herein, with respect to previous attempts [22]. The pushover curve provides a prediction of the load capacity of the structure within 10% accuracy and a reliable prediction of the residual strength.

Regarding the analysis under cyclic loading which was allowed to run up for a reasonable duration of time - two cycles of approximately 5mm and 10mm
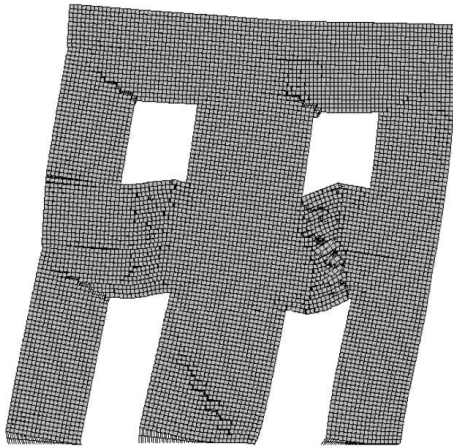

Fig. 22 Perforated wall: plan of building, hierarchic partitioning of Wall D and applied loads (P.B=Partition Boundary)

Fig. 24 Perforated wall: deformed shape at the end of the cyclic analysis
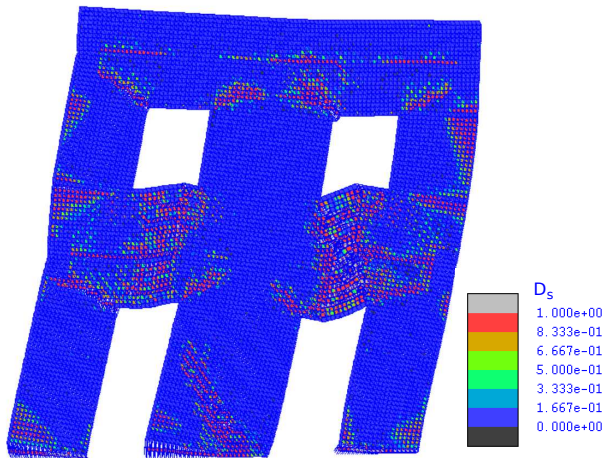

Fig. 25 Perforated wall: damage developed in the interface elements at the end of the cyclic analysis

were completed and are presented in Fig. 23. Strength degradation that agrees with the experimental curve, especially at the reloading stage of the second cycle, is observed. Furthermore, when cyclic loading is applied, the displacement drift corresponding to the maximum strength of the wall agrees with the experimental value (10mm). The stiffness degradation upon load reversal predicted in the numerical curve is lower than that of the experimental curve. This discrepancy is probably linked to the reduced number of cycles performed in the numerical simulation, due to the increased computational time required for the analysis. The time required for further cycles with the computational resources currently available is prohibitive, which highlights a practical limit for the proposed approach with respect to the size of the model using current computational resources.

Finally, Fig. 24 and 25 depict respectively the cracking pattern and the damage developed in the interfaces at the end of the cyclic analysis. Both results reveal that the predicted damage of the structure is located at the same regions as in the experimental observations reported in [38].

5 Conclusion

A new constitutive model for the behaviour of cohesive interfaces in mesoscale representation of masonry is proposed. The mesoscale approach consists of elastic solid elements for the masonry blocks and nonlinear cohesive interface elements representing the mortar joints and the potential failure surfaces of the bricks. The proposed constitutive model provides an accurate description of the key defining characteristics of the physical behaviour of the interfaces in a simple and robust way. The use of a hierarchic partitioning framework has increased the efficiency of the strategy and reduced the computational cost.

Experimental-numerical comparisons have demonstrated the potential of this approach for the simulation of URM structures under quasi-static and dynamic loading conditions. Discrepancies observed between the real response and the numerical prediction can be attributed to the uncertainty in the identification of certain material parameters and to the simplifications in the yield surface, the damage evolution and the loading-unloading path. Those characteristics can be further investigated as the conceptual simplicity of the approach allows localised enhancements without compromising numerical robustness.

Notably, it has been shown that relatively large scale components can be analysed in a 3D framework with reliable results, which opens numerous possibilities in the advanced study of masonry structures. The existence of an upper limit on the size of the model that can be analysed currently with the mesoscale model has been shown in Section 4.4; in this scale, conclusions can be drawn for the structure under monotonic load, but only a limited number of load reversals can be considered. For such cases, alternative methods can be explored for increased efficiency, such as the modelling of a small assembly of bricks with one solid element with homogenised characteristics.

In conclusion, the proposed strategy can be a useful tool for the investigation of the behaviour of URM structures under cyclic loading.

acknowledge the support of the HPC Service of Imperial College London for the computational resources provided for the numerical analyses performed here.

References

1. Magenes, G., Fontana, A.: Simplified non-linear seismic analysis of masonry buildings. In: Proc. Br. Masonry Soc. No. 8, pp. 190–195 (1998)
2. Lagomarsino, S., Penna, A., Galasco, A., Cattari, S.: Tremuri program: an equivalent frame model for the non-linear seismic analysis of masonry buildings. Engineering Structures **56**, 1787–1799 (2013)
3. Caliò, I., Marletta, M., Pantò, B.: A new discrete element model for the evaluation of the seismic behaviour of un-reinforced masonry buildings. Engineering Structures **40**, 327–338 (2012)
4. Lourenço, P.B., Rots, J.G., Blaauwendraad, J.: Continuum model for masonry: parameter estimation and validation. Journal of Structural Engineering **124**(6), 642–652 (1998)
5. Calderini, C., Lagomarsino, S.: Continuum model for in-plane anisotropic inelastic behavior of masonry. Journal of structural engineering **134**(2), 209–220 (2008)
6. Pelà, L., Cervera, M., Roca, P.: An orthotropic damage model for the analysis of masonry structures. Construction and Building Materials **41**, 957–967 (2013)
7. Hillerborg, A., Modéer, M., Petersson, P.E.: Analysis of crack formation and crack growth in concrete by means of fracture mechanics and finite elements. Cement and concrete research **6**(6), 773–781 (1976)
8. Carol, I., López, C.M., Roa, O.: Micromechanical analysis of quasi-brittle materials using fracture-based interface elements. International Journal for Numerical Methods in Engineering **52**(1-2), 193–215 (2001)
9. Caballero, A., Willam, K., Carol, I.: Consistent tangent formulation for 3d interface modeling of cracking/fracture in quasi-brittle materials. Computer Methods in Applied Mechanics and Engineering **197**(33), 2804–2822 (2008)
10. Lourenço, P.B., Rots, J.G.: Multisurface interface model for analysis of masonry structures. Journal of engineering mechanics **123**(7), 660–668 (1997)
11. Snozzi, L., Molinari, J.F.: A cohesive element model for mixed mode loading with frictional contact capability. International journal for numerical methods in engineering **93**(5), 510–526 (2013)
12. Oliveira, D.V., Lourenço, P.B.: Implementation and validation of a constitutive model for the cyclic behaviour of interface elements. Computers & structures **82**(17), 1451–1461 (2004)
13. Aref, A.J., Dolatshahi, K.M.: A three-dimensional cyclic meso-scale numerical procedure for simulation of unreinforced masonry structures. Computers & Structures **120**, 9–23 (2013)
14. Sacco, E., Toti, J.: Interface elements for the analysis of masonry structures. International Journal for Computational Methods in Engineering Science and Mechanics **11**(6), 354–373 (2010)
15. Ragueneau, F., Dominguez, N., Ibrahimbegovic, A.: Thermodynamic-based interface model for cohesive brittle materials: application to bond slip in rc structures. Computer Methods in Applied Mechanics and Engineering **195**(52), 7249–7263 (2006)
16. Spada, A., Giambanco, G., Rizzo, P.: Damage and plasticity at the interfaces in composite materials and structures. Computer Methods in Applied Mechanics and Engineering **198**(49), 3884–3901 (2009)
17. Albarella, M., Serpieri, R., Alfano, G., Sacco, E.: A 3d multiscale cohesive zone model for quasi-brittle materials accounting for friction, damage and interlocking. European Journal of Computational Mechanics **24**(4), 144–170 (2015)
18. Gambarotta, L., Lagomarsino, S.: Damage models for the seismic response of brick masonry shear walls. part i: the mortar joint model and its applications. Earthquake engineering & structural dynamics **26**(4), 423–439 (1997)
19. Grassl, P., Rempling, R.: A damage-plasticity interface approach to the meso-scale modelling of concrete subjected to cyclic compressive loading. Engineering Fracture Mechanics **75**(16), 4804–4818 (2008)
20. Macorini, L., Izzuddin, B.: Nonlinear analysis of masonry structures using mesoscale partitioned modelling. Advances in Engineering Software **60**, 58–69 (2013)
21. Izzuddin, B.A.: An enhanced co-rotational approach for large displacement analysis of plates. International Journal for Numerical Methods in Engineering **64**(10), 1350–1374 (2005). DOI 10.1002/nme.1415. URL http://dx.doi.org/10.1002/nme.1415
22. Macorini, L., Izzuddin, B.: A non-linear interface element for 3d mesoscale analysis of brick-masonry structures. International Journal for numerical methods in Engineering **85**(12), 1584–1608 (2011)
23. Macorini, L., Izzuddin, B.: Enhanced mesoscale partitioned modelling for unreinforced masonry structures. In: Proceedings of the 14th International Conference on Civil, Structural and Environmental Engineering Computing. September 3-6, Cagliari-Sardinia-Italy (2013)
24. Jokhio, G., Izzuddin, B.: A dual super-element domain decomposition approach for parallel nonlinear finite element analysis. International Journal for Computational Methods in Engineering Science and Mechanics **16**(3), 188–212 (2015)
25. Izzuddin, B.A., Jokhio, G.A.: Mixed-dimensional coupling for parallel partitioned nonlinear finite-element analysis. Journal of Computing in Civil Engineering p. 04016062 (2016)
26. Atkinson, R., Amadei, B., Saeb, S., Sture, S.: Response of masonry bed joints in direct shear. Journal of Structural Engineering **115**(9), 2276–2296 (1989)
27. Simo, J.C., Hughes, T.J.: Computational inelasticity, vol. 7. Springer Science & Business Media (2006)
28. Lourenço, P.B., Ramos, L.ı.s.F.: Characterization of cyclic behavior of dry masonry joints. Journal of Structural Engineering **130**(5), 779–786 (2004)
29. Reinhardt, H.W.: Fracture mechanics of an elastic softening material like concrete. HERON, 29 (2), 1984 (1984)
30. Oliveira, D.V., Lourenço, P.B., Roca, P.: Cyclic behaviour of stone and brick masonry under uniaxial compressive loading. Materials and Structures **39**(2), 247–257 (2006). DOI 10.1617/s11527-005-9050-3. URL http://dx.doi.org/10.1617/s11527-005-9050-3
31. Izzuddin, B.: Nonlinear dynamic analysis of framed structures. Ph.D. thesis, Imperial College, University of London (1991)

32. Anthoine, A., Magonette, G., Magenes, G.: Shear-compression testing and analysis of brick masonry walls. In: Proceedings of the 10th European conference on earthquake engineering, pp. 1657–62 (1995)
33. Binda, L., Tiraboschi, C., Mirabella Roberti, G., Baronio, G., Cardani, G.: Measuring masonry material properties: detailed results from an extensive experimental research, part i: Tests on masonry components. Rep **5** (1996)
34. Griffith, M.C., Lam, N.T., Wilson, J.L., Doherty, K.: Experimental investigation of unreinforced brick masonry walls in flexure. Journal of Structural Engineering **130**(3), 423–432 (2004)
35. Doherty, K.T.: An investigation of the weak links in the seismic ioad path of unreinforced masonry buildings. Ph.D. thesis, Faculty of Engineering at The University of Adelaide for the Degree of Doctor of Philosophy Department of Civil and Environmental Engineering, The University of Adelaide (2000)
36. Milani, G.: 3d upper bound limit analysis of multi-leaf masonry walls. International Journal of Mechanical Sciences **50**(4), 817–836 (2008)
37. Griffith, M.C., Vaculik, J., Lam, N., Wilson, J., Lumantarna, E.: Cyclic testing of unreinforced masonry walls in two-way bending. Earthquake Engineering & Structural Dynamics **36**(6), 801–821 (2007)
38. Magenes, G., Kingsley, G.R., Calvi, G.M.: Seismic testing of a full-scale, two-story masonry building: test procedure and measured experimental response. Consiglio nazionale delle ricerche, Gruppo nazionale per la Difesa dai terremoti (1995)